Native defects and impurity band behavior in half-Heusler thermoelectric NbFeSb

Journal:	*Physical Chemistry Chemical Physics*
Manuscript ID	CP-ART-07-2018-004287.R1
Article Type:	Paper
Date Submitted by the Author:	06-Aug-2018

Complete List of Authors:	Tian, Yefan; Texas A&M University, Department of Physics and Astronomy Zhu, Hangtian; University of Houston, Department of Physics Ren, Wuyang; University of Electronic Science and Technology of China, State Key Lab Elect Thin Films & Integrated Devic; University of Houston, Department of Physics Ghassemi, Nader; Texas A&M University, Department of Physics and Astronomy Conant, Emily; Texas A&M University, Department of Physics and Astronomy Wang, Zhiming; University of Electronic Science and Technology of China, Ren, Zhifeng; University of Houston, Department of Physics; University of Houston, Texas Center for Superconductivity at the University of Houston Ross, Joseph; Texas A&M University, Department of Physics and Astronomy; Texas A&M University, Department of Material Science and Engineering

Journal Name

ARTICLE TYPE

Cite this: DOI: 10.1039/xxxxxxxxxx

Native defects and impurity band behavior in half-Heusler thermoelectric NbFeSb†

Yefan Tian,[a] Hangtian Zhu,[b] Wuyang Ren,[b,c] Nader Ghassemi,[a] Emily Conant,[a] Zhiming Wang,[c] Zhifeng Ren,[b,d] and Joseph H. Ross, Jr.*[a,e]

Received Date
Accepted Date

DOI: 10.1039/xxxxxxxxxx

www.rsc.org/journalname

To investigate the electronic behavior and magnetic properties of NbFeSb, we have performed ^{93}Nb NMR, specific heat and magnetic measurements on NbFeSb samples heat treated at high temperatures. Magnetic measurements, combined with an observed Schottky anomaly and changes in the NMR line width indicate the presence of a 0.2% concentrated native magnetic defect in stoichiometric NbFeSb samples. The origin of these native defects is believed due to Fe antisites on Nb sites. In addition, NMR shift and spin-lattice relaxation results below 200 K reveal a Korringa-like response indicating heavily-doped p-type behavior due to native defects. Above 280 K this goes over to an activated behavior indicating the presence of an impurity band, empty at low temperatures, which is located around 0.03 eV above valence band maximum.

1 Introduction

In recent years, the half-Heusler semiconductor NbFeSb has been of particular interest due to its excellent thermoelectric performance within the realm of earth abundant thermoelectric materials[1]. With various elements doped or substituted, NbFeSb exhibits a high power factor[2,3]. To further understand the influence of defects on half-Heusler materials, several different types of impurities have been explored and studied within the half-Heusler family, including interstitials and antisites[4–6], and substitutions[7,8]. Defects can control the transport properties of half-Heusler compounds, thus enabling the electronic behaviors to be tuned. However, native defects can also counteract the desired effects or otherwise degrade the electronic response. The defect issue has been explored experimentally for several compounds, such as ZrNiSn and TiCoSb[9–11].

The half-Heusler family, as one of the most fascinating intermetallic systems, has gained considerable attention in recent decades due to their unique transport and magnetic behaviors. These materials have general formula XYZ (X and Y representing transition metals, Z a tetrel or pnictogen element)[12–14], and can be formally derived from the cubic Heusler phases X_2YZ by removing one of the two equivalent X atoms, leading to a structural vacancy. The ideal valence electron concentration (VEC) of half-Heusler compounds is 8 or 18 electrons per formula unit[15–19], with semiconducting or semimetallic behavior often observed with VEC = 18[13–16,20]. With a rich combination of chemical elements, this feature leads to interesting properties, from non-magnetic semiconductors to ferromagnetic half metals, as well as other anomalous behavior, including strongly correlated electrons and topological insulator behavior[21–23]. Often, for high-ZT thermoelectric materials, these must be heavily doped, however, it is important to study intrinsic materials to better understand the underlying electronic properties of NbFeSb-based thermoelectric materials in order to optimize the performance. Furthermore, in NbFeSb there are significant differences in reported properties, for example for the band gap[24], and better understanding of such fundamental features will help to build a more efficient material design process.

To analyze the underlying electronic and magnetic properties of NbFeSb, we performed a series of measurements aimed at better understanding and eventual utilization of these materials. In results from magnetic, nuclear magnetic resonance (NMR) and specific heat measurements, we demonstrate the presence of several native defects in NbFeSb resulting in its very low native mobility and an enhanced carrier density above room temperature due to an impurity band, providing a better understanding of native defects in off-stoichiometric samples, which play an important role in designing new NbFeSb-based thermoelectric materials.

[a] Department of Physics and Astronomy, Texas A&M University, College Station, TX 77843, USA. E-mail: jhross@tamu.edu
[b] Department of Physics, University of Houston, Houston, TX 77204, USA.
[c] Institute of Fundamental and Frontier Sciences, University of Electronic Science and Technology of China, Chengdu 610054, China.
[d] Texas Center for Superconductivity at the University of Houston, University of Houston, Houston, TX 77204, USA.
[e] Department of Materials Science and Engineering, Texas A&M University, College Station, TX 77843, USA.

† Electronic Supplementary Information (ESI) available: Stretched-exponential spin-lattice relaxation analysis. See DOI: 10.1039/b000000x/

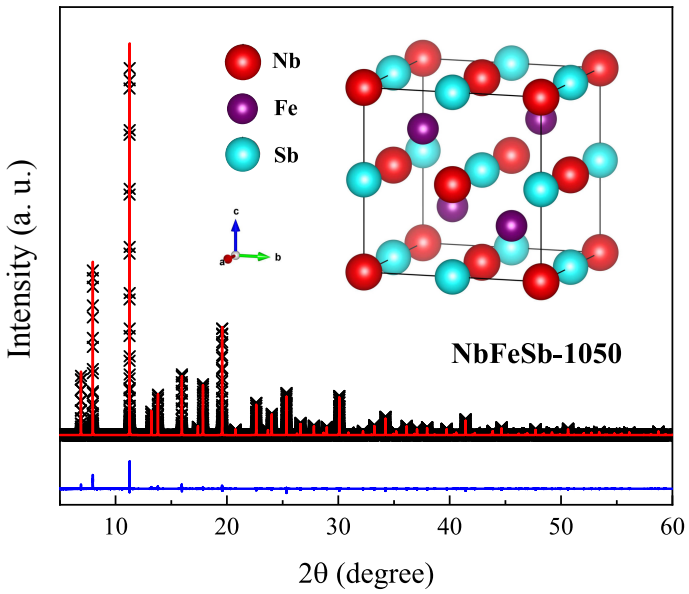

Fig. 1 Powder XRD results for NbFeSb-1050 sample at 295 K with Rietveld refinement and difference plots. The half-Heusler structure is also shown superposed.

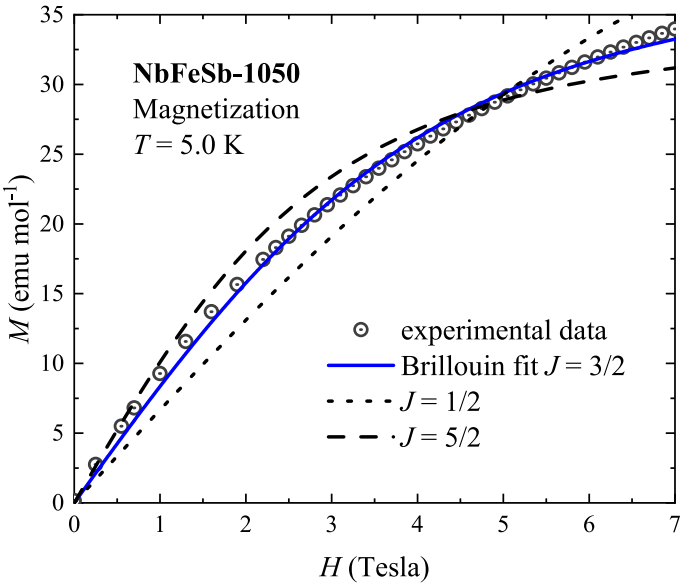

Fig. 2 Sample NbFeSb-1050 magnetization vs magnetic field measured at 5 K. Brillouin function fit is shown with $J = 1/2$ and $J = 5/2$ curves for comparison. Error bars are too small to be seen.

2 Sample preparation and experimental methods

Three NbFeSb samples were prepared by an arc melting, ball milling, and hot pressing process. Stoichiometrically weighed raw elements, adjusted for Sb loss to give 1:1:1 atomic ratios after processing, were melted several times in an Ar-protected chamber to form homogeneous ingots. These were loaded into an Ar-filled stainless steel jar and ball milled for 3 h. The ball milled powder was finally consolidated into 13 mm diameter disks via hot pressing. The hot pressing temperatures were 1050, 1000, and 900°C with holding for 2 min. Here we denoted these samples as NbFeSb-1050, NbFeSb-1000, and NbFeSb-900 respectively.

High-resolution powder X-ray diffraction (XRD) data were collected at the Advanced Photon Source, Argonne National Laboratory using an X-ray wavelength of 0.412703 Å. NbFeSb-1050 results are shown in Fig. 1. Rietveld refinements were performed using the GSAS-II software package, and the lattice constant 5.9497 Å was obtained, with identical results for the other two samples within 0.0001 Å. This is close to the value 5.9522 Å reported in other work[25]. The XRD results showed no sign of secondary phase.

Magnetic measurements were performed using a Quantum Design MPMS superconducting quantum interference device magnetometer. Specific heat and transport measurements were conducted using a Quantum Design Physical Property Measurement System. ^{93}Nb NMR experiments were carried out by applying a custom-built pulse spectrometer at a fixed magnetic field about 9 T using shift standard $NbCl_5$ in acetonitrile, with positive shifts here denoting paramagnetic sign. Magic angle spinning (MAS) NMR measurements were performed using a Bruker Advance 400 spectrometer. To avoid multi-exponential effects due to quadrupole splitting, NMR T_1 measurements were performed using a saturating comb of pulses.

Resistivity and Hall measurements were performed at 300 K, on a piece of the NbFeSb-1050 sample cut into a Hall bar. The measured resistivity is 0.2 Ω cm, with Hall results corresponding to a hole density of 9×10^{19} cm^{-3}, assuming no compensation effects. This indicates a very small room-temperature hole mobility of about 0.3 cm^2 V^{-1} s^{-1}, considerably smaller than found in Ti-substituted NbFeSb[1]. A very small mobility was previously noted for unsubstituted NbFeSb[24,26], apparently due to nearness to a localization transition. For example, assuming a hole effective mass of 2 m_e[27] and a dielectric constant $\varepsilon = 30$ similar to that of TiNiSn[28], the Mott condition ($a_B n_c^{1/3} \approx 0.25$)[29] corresponds to a carrier density $n_c = 3\times10^{19}$ cm^{-3}.

3 Results and analysis

3.1 Magnetic measurements

Magnetization vs T results proved difficult to separate from a small ferromagnetic response, likely due to a surface oxide, even though representing a several orders of magnitude smaller moment density than the defects discussed below. However, M vs H measurements revealed dilute paramagnetic defects, as shown at $T = 5$ K for NbFeSb-1050 in Fig. 2. To analyze for the local magnetic moments, data were fit to

$$M = N_A c g J \mu_B B_J(x), \quad (1)$$

where N_A is Avogadro's constant, c is the concentration of defects, and $B_J(x)$ is a Brillouin function with $x = \frac{g\mu_B JB}{k_B T}$. Assuming $g = 2$, expected for transition ions, the fitted $J = 1.53$ indicates a single, dominant type of defect with $J = 3/2$. Fixing $J = 3/2$, the fit gave $c = 0.00221$ per formula unit with $g = 2.026$. The corresponding effective moment is $p_{\rm eff} = g\sqrt{J(J+1)}\mu_B = 3.923\ \mu_B$.

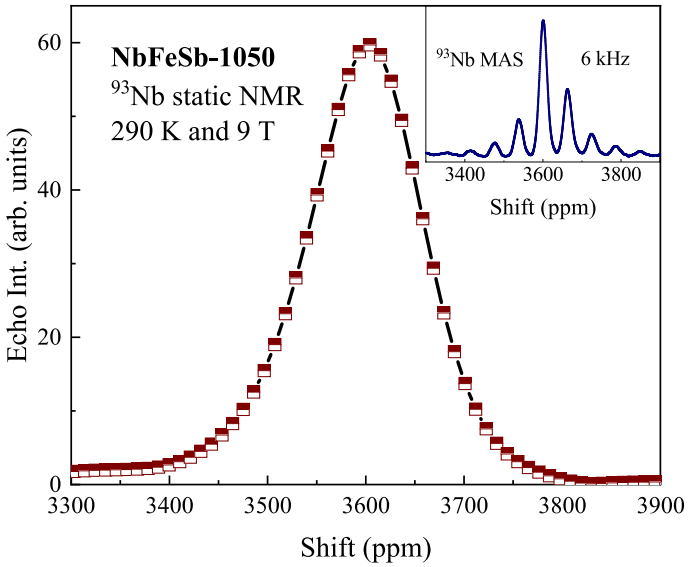

Fig. 3 ^{93}Nb static NMR spectrum of NbFeSb-1050 at 290 K. Inset: Magic angle spinning spectrum with rotation speed 6 kHz.

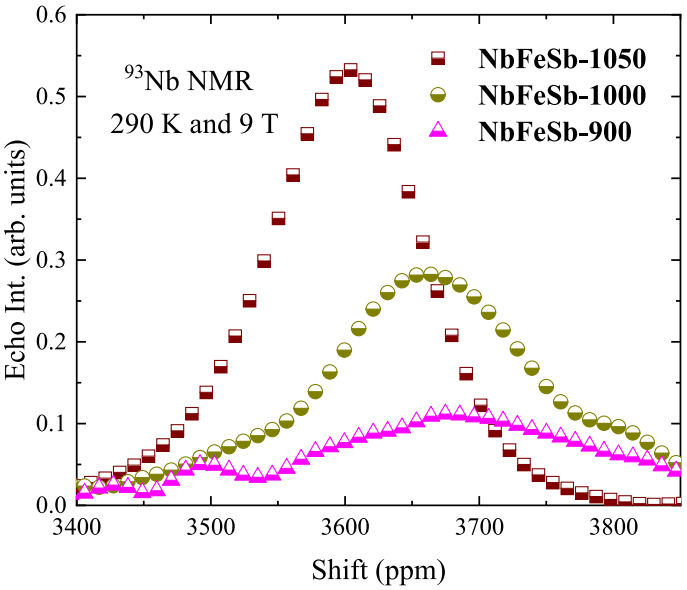

Fig. 4 ^{93}Nb static NMR spectra of NbFeSb samples prepared in hot pressing temperatures 1050, 1000, and 900°C, normalized to sample mass.

3.2 NMR measurements

3.2.1 NMR line shape

The static 290 K ^{93}Nb NMR spectrum shown in Fig. 3 demonstrates a very large shift of 3600 ppm for NbFeSb-1050, which is outside the typical range of Nb chemical shifts[30], presumably due to a large paramagnetic response of Nb *d* orbitals appearing in both the valence and conduction bands. The inset of Fig. 3 shows room temperature MAS results, indicating a narrow intrinsic line with no sign of splitting or inhomogeneous broadening, an indication that the site occupations are well ordered, with few local atomic interchanges[31–33]. To further examine whether there could be a small peak within the observed resonance, corresponding to additional local Nb environments such as reported for Mg on octahedral sites in half-Heusler MgAgAs[33], we examined the first moment of the static line measured in the MAS probe. Its position is identical to that of the MAS isotropic peak, to less than the 1 ppm first moment uncertainty. Thus there is no evidence for any significant population of Nb atoms located on such additional sites, with a detection limit for these measurements on order of 1%.

Line shapes of all samples are shown in Fig. 4 with shifts increasing to 3680 ppm for NbFeSb-900. The inset of Fig. 5 shows the center of mass shift vs T for the NbFeSb-1050 sample. At low temperatures there is a decrease corresponding to the interaction of carriers with the localized defects, and at high temperatures the increase corresponds to an enhanced Knight shift (see Discussion section).

In cubic NbFeSb, we expect no quadrupole shifts for an ideal crystal. However, spectral amplitudes at 290 K vary considerably between samples (Fig. 4), with the observed NbFeSb-900 line smaller by a factor 4.8 (scaled according to sample mass) than for NbFeSb-1050. This is close to the factor of $[I(I+1)+1/4]^{1/2}=5$ for the central transition ($m=1/2$ to -1/2) for $I=9/2$ ^{93}Nb, as the quadrupole satellite resonances collapse toward the central transition; see for example reported by Ageev *et al.*[34]. This indicates that random electric field gradients due to lattice strains are significantly reduced in sample NbFeSb-1050.

3.2.2 NMR line width

The low-temperature broadening of the ^{93}Nb NMR lines also supports the magnetic defect picture described above. To probe this behavior, the full width at half maximum (FWHM) was recorded vs temperature. The results correspond to a Curie-type behavior as shown in Fig. 5. With no associated Curie-law shifts, this corresponds to the effect of dilute paramagnetic defects.

Walstedt *et al.*[35] calculated such effects. For the case where fluctuation of the impurity spins is rapid compared with the NMR splittings, the line width is proportional to the average spin moment. According to this theory, substitutional defects having spin S and concentration c will produce a FWHM, $\Delta\nu$, which can be expressed[35,36],

$$\Delta\nu = \frac{2}{9\sqrt{3}}\frac{c\gamma_n g\mu_B}{V}\langle S_z(T)\rangle, \qquad (2)$$

where $\langle S_z(T)\rangle = \frac{g^2J(J+1)\mu_B B}{3k_BT}$ is the average spin component in the field direction, and V is the volume per formula unit. We used $g=2$ and $J=3/2$, obtained from magnetic measurements. The fit vs T, shown in Fig. 5, yields an impurity concentration of 0.0022 with a T-independent background 14.4 kHz. These results are consistent with results from the other methods, and confirm that the defects are randomly distributed in the sample.

3.2.3 Spin-lattice relaxation

T_1^{-1} results from saturation-recovery experiments are shown in Fig. 6, obtained from fitting a recovery curve $S(t)\propto e^{-(t/T_1)^\beta}$, setting $\beta=1$. Alternatively, allowing β to vary yielded $\beta\approx 1$ near room temperature and at low temperatures, but smaller values

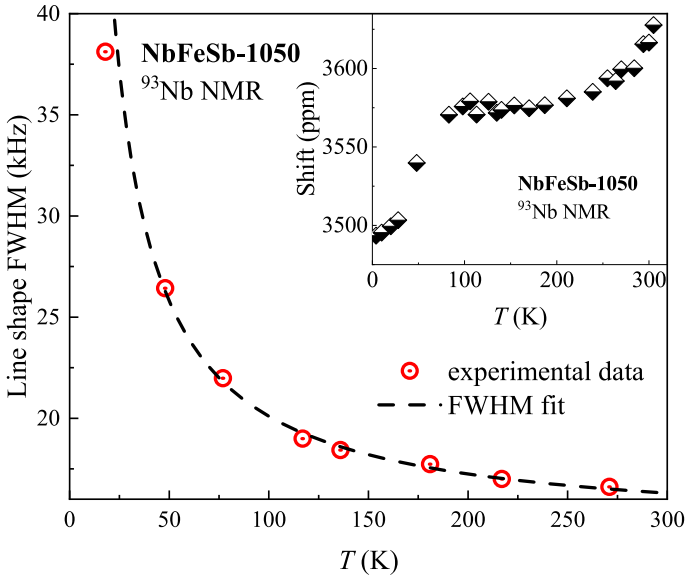

Fig. 5 Variation of ^{93}Nb FWHM line width vs temperature for NbFeSb-1050. Dashed line: Curie-like function fitted as described in the text. Inset: shift vs temperature.

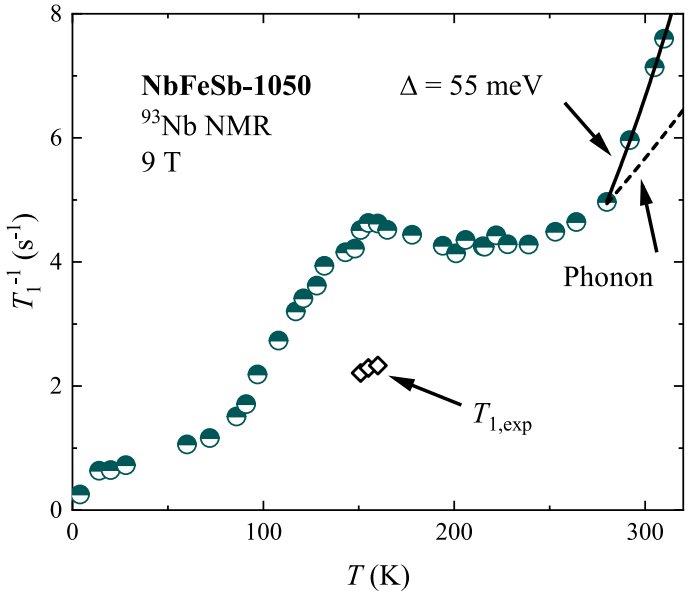

Fig. 6 Temperature dependence of ^{93}Nb spin-lattice relaxation rates, along with $T_{1,\mathrm{exp}}$ obtained as described in the text. Error bars are approximately the size of the symbols.

in the vicinity of the peak, for example $\beta = 0.85$ at 155 K. This result is consistent with a contribution due to fluctuating defects, with the peak occurring when the maximum in the fluctuation spectrum matches the NMR frequency, as also observed in other Fe-containing Heusler alloys[37].

If nuclear spin-diffusion is not important, relaxation due to uncorrelated local moments is found to approach a stretched exponential, $S(t) \propto e^{(-t/\tau_1)^{1/2}}$. This occurs because of an inhomogeneous distribution of local relaxation rates. For a concentration c per unit volume of effective moments p, the exponential factor is[38],

$$\tau_1^{-1/2} = 4.7\frac{p\mu_B\gamma_n c}{\sqrt{\omega}}\left(\frac{\omega\tau_c}{1+\omega^2\tau_c^2}\right)^{1/2}, \qquad (3)$$

where ω is the NMR frequency, and a single Debye-type correlation time τ_c has been assumed to apply to the local moments. When $\omega = \tau_c^{-1}$, a maximum of τ_1^{-1} is reached,

$$(\tau_1^{-1})_{\max} = 11.05\frac{p^2\mu_B^2\gamma_n^2 c^2}{\omega}. \qquad (4)$$

For the concentration 0.0022 per formula unit of defects detected here, this yields, $(\tau_1^{-1})_{\max} = 1.5\ \mathrm{s}^{-1}$.

Since the paramagnetic fluctuation peak sits atop an overall increase in T_1^{-1} vs temperature, we assumed a relaxation function for each temperature given by $S(t) = S_0\exp(-t/T_{1,\mathrm{exp}})\sum_i c_i\exp[-t/(T_{1s})_i]$, where $\exp(-t/T_{1,\mathrm{exp}})$ is the overall exponential relaxation function, c_i and $(T_{1s})_i$ represent a continuous distribution generating the stretched function $\exp[-(t/\tau_1)^{1/2}]$. We obtained a numerical summation equivalent to the latter distribution, scaled by a single parameter corresponding to τ_1, and fitted the relaxation data to obtain $T_{1,\mathrm{exp}}$ and τ_1 near the observed peak (See Supplemental Material for details). Results agree with the calculated $\tau_1^{-1} = 1.5\ \mathrm{s}^{-1}$ within experimental error, so to better identify the underlying exponential behavior we fixed $\tau_1^{-1} = 1.5\ \mathrm{s}^{-1}$, and fitted for $T_{1,\mathrm{exp}}$ at three temperatures close to the maximum position. This yielded the results 2.21(11), 2.29(16) and 2.33(12) s^{-1}, at 151, 155 and 160 K respectively, also plotted in Fig. 6. As described in the Discussion, these agree with a Korringa process for the overall relaxation term, as expected in the case of sufficient carrier density to produce metallic behavior.

In the upper end of the temperature range, both K and T_1^{-1} show a rapid increase. Normally, due to phonons, T_1^{-1} approaches a T^2 behavior[39] (dashed curve in Fig. 6), with little effect on the NMR shift. Instead, the T_1^{-1} data could be fitted to

$$T_1^{-1} = CT^2e^{\Delta/k_BT}, \qquad (5)$$

with $\Delta = 55$ meV. Setting $\Delta = E_g/2$, this is the expected function[40] for an intrinsic semiconducting regime, however this assumes a gap (E_g) much larger than kT, with the chemical potential (μ) close to the mid-gap. Starting in the metallic regime with μ at the band-edge, Δ should be closer to E_g, and in numerical simulations for various band-edge effective masses the observed steep rise in T_1^{-1} was consistent with E_g of approximately 0.03 eV. With computed band gaps[1,17,27,41–43] in the range 0.51-0.78 eV, and an activated electrical conductivity corresponding to $E_g = 0.51$ eV

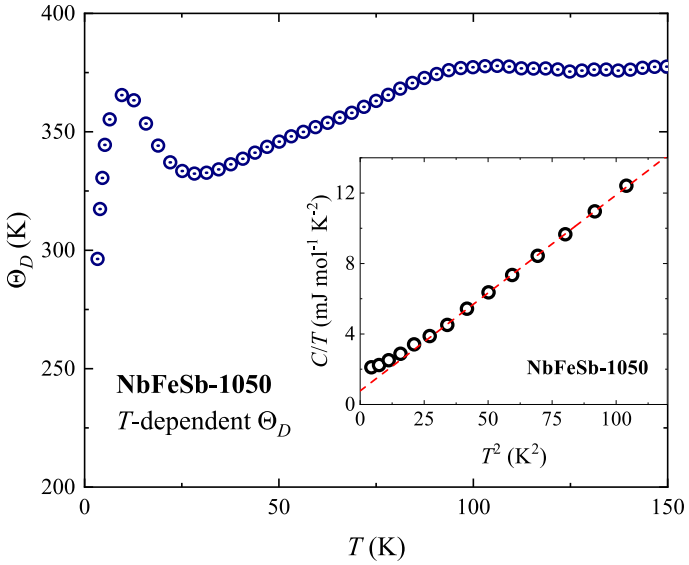

Fig. 7 Debye temperature extracted from NbFeSb-1050 specific heat, for $H = 0$ T. Inset: C/T vs T^2 between 2 and 10 K, with fit described in the text.

identified above 600 K[1], it is unlikely that this very small result corresponds to the entire gap. Therefore, we conclude that the activation energy corresponds to an isolated impurity band within the NbFeSb gap, a situation recognized to play an important role in the behavior of other half-Heusler thermoelectric materials, due to native defects even in nominally intrinsic materials[4,44].

3.3 Specific heat

Specific heats of the NbFeSb-1050 and NbFeSb-900 samples were measured from 1.8-300 K in magnetic fields $H = 0$, 5 and 9 T. The zero-field C/T vs T^2 below 11 K for NbFeSb-1050, shown in the inset of Fig. 7, shows linear behavior with a small upturn at low temperature. The upturn may be due to local moment interaction with carriers. A fit to $C/T = \gamma + \beta T^2$ yields $\gamma = 0.77$ mJ mol^{-1} K^{-2} and $\beta = 0.11$ mJ mol^{-1} K^{-4}. The Debye temperature obtained from $\Theta_D = (12nR\pi^4/5\beta)^{1/3}$, where n is the number of atoms per formula unit and R is the ideal gas constant, is $\Theta_D = 375$ K. A similar fit for NbFeSb-900 yields $\gamma = 1.21$ mJ mol^{-1} K^{-2}.

Fig. 7 shows the Debye temperature fitted by solving the standard integral equation,

$$C = 9nR\left(\frac{T}{\Theta_D}\right)^3 \int_0^{\Theta_D/T} \frac{x^4 e^x}{(e^x-1)^2} dx, \qquad (6)$$

As shown, there is a plateau of Θ_D about 375 K, consistent with the low-temperature results and other reports[24].

Field-dependent results for NbFeSb-900 and NbFeSb-1050 yield a small low-temperature difference shown in Fig. 8(a) and 8(b), subtracting the 0 T from 5 T and 9 T data. For independent moments with $J \neq 1/2$, the corresponding specific heat anomaly is generalized to the multilevel Schottky function[45]:

$$C_m = cR\left[\frac{x^2 e^x}{(e^x-1)^2} - \frac{[(2J+1)x]^2 e^{(2J+1)x}}{(e^{(2J+1)x}-1)^2}\right], \qquad (7)$$

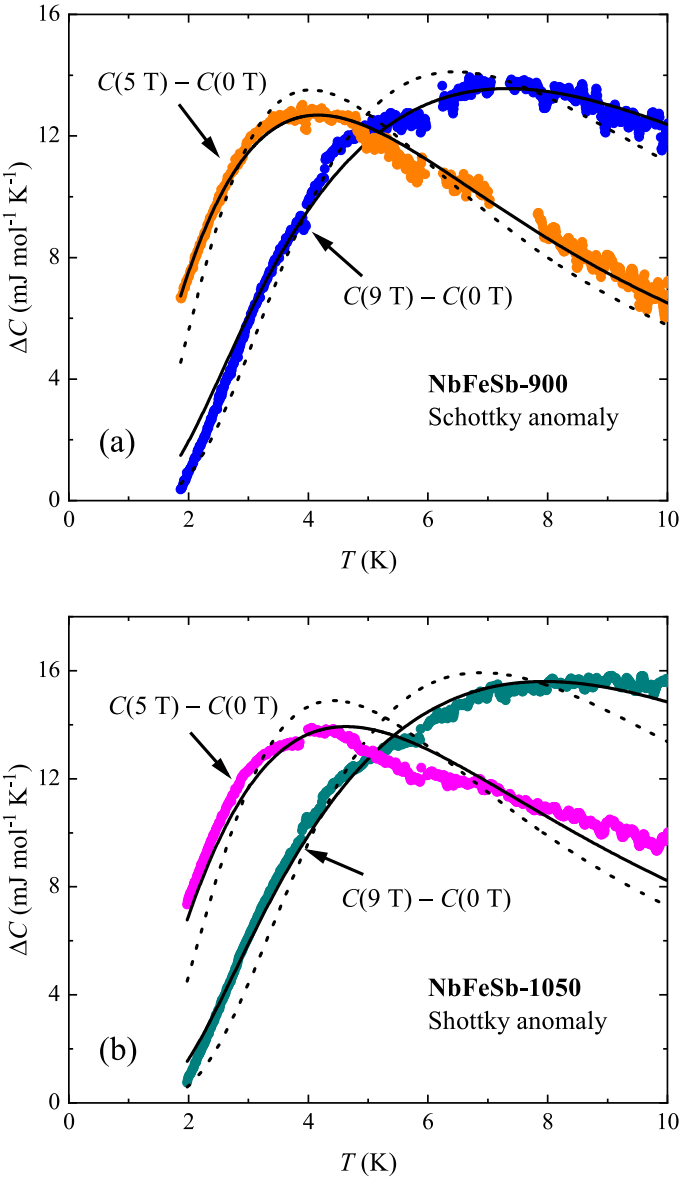

Fig. 8 (a) NbFeSb-900 and (b) NbFeSb-1050 specific heat differences vs T. Solid curves: H = 5 and 9 T $J = 3/2$ multilevel Schottky anomalies; dotted curves: $J = 1/2$ fits for comparison.

where $x = \frac{g\mu_B H}{k_B T}$. With $J = 3/2$, this function provided good agreement. Curves for $J = 1/2$ corresponding to a standard two-level Schottky function are also shown in Fig. 8, however the goodness of fit is not as favorable. Fitted results are shown in Table 1.

Table 1 Specific heat parameters, with $J = 3/2$, and defect concentration c per formula unit.

NbFeSb	ΔC	g-factor	c
1050	$C(9\text{ T}) - C(0\text{ T})$	2.058 ± 0.003	0.00253(3)
900	$C(5\text{ T}) - C(0\text{ T})$	1.941 ± 0.003	0.00205(2)
900	$C(9\text{ T}) - C(0\text{ T})$	1.897 ± 0.004	0.00219(3)

4 Discussion

According to first principles band structure calculations, NbFeSb is predicted to be a narrow-gap semiconductor, with an indirect gap in the range 0.51-0.78 eV[1,17,27,41–43], up to 1.77 eV reported by Çoban *et al.*[46]. The properties observed here can be interpreted by the following picture: the as-grown material is nonmagnetic with a 0.2% paramagnetic defects per formula unit in a p-type matrix. A consistent measurement of the defect concentrations is provided by different methods, as summarized in Table 2. The transport properties observed here are similar to those of the unsubstituted material reported by Tavassoli *et al.*[24], and thus we expect that this behavior is typical for native defects in NbFeSb.

Table 2 Summary for NbFeSb-1050 by different methods.

method	defect concentration (per formula unit)
Magnetization	0.00221
NMR FWHM	0.00223
Specific heat[a]	0.00253

[a] From $C(9\text{ T}) - C(0\text{ T})$.

The narrow observed NMR line widths, and collapse of the quadrupole-split satellites in the highest-temperature processed sample NbFeSb-1050, demonstrate that samples prepared this way are very well ordered. The unchanging lattice constant vs processing conditions indicates little or no variation in composition, while the NMR quadrupole broadening process is very sensitive to site-occupation disorder. As shown above, the NMR shift results indicate a single local environment for Nb, precluding the presence of a large concentration of Nb antisites or similar defects. This also agrees with results[24] limiting NbFeSb to a narrow composition region of the ternary phase diagram, and with stabilization according to the 18-electron rule for half-Heusler compounds[15–19].

To better understand the temperature-dependence identified for NbFeSb-1050, note that the NMR shift (inset of Fig. 5) consists of a sum of the chemical shift (δ), due to the orbital susceptibility, and the Knight shift (K), connected to the paramagnetic spin susceptibility[47], with K the most important source of T dependence. With the valence band (VB) edge dominated by Fe and Nb d orbitals[27,41,42], K would be due to core-polarization, with a negative sign[48] for Nb. Based on the linear heat capacity at low temperatures, the degenerate statistics result[49] $\gamma = \frac{\pi^2}{3} k_B^2 g(\varepsilon_F)$ gives a Fermi level density of states $g(\varepsilon_F) = 0.33$ states/eV per formula unit. Using the room-temperature Hall-derived hole density $n_h = 9 \times 10^{19}$ cm^{-3}, and an effective mass approximation[49] for which $g(\varepsilon_F) = \frac{3}{2}(n_h/\varepsilon_F)$ and $\varepsilon_F = \frac{\hbar^2}{2m^*}(3\pi^2 n_h)^{2/3}$, we obtain $m^* = 3.4\ m_e$ and a Fermi temperature $T_F = 250$ K. The effective mass is close to computed values, for example 4.5 m_e based on mBJ-based DFT[27], distributed among 4 degenerate VB maxima at the L position in k-space.

In absence of correlation effects, in terms of the Pauli susceptibility (χ_P), the Knight shift is given by $K = H^{\rm HF}\chi_P/\mu_B = H^{\rm HF}\mu_B g \varepsilon_F$. Here $H^{\rm HF}$ is the hyperfine field, assumed equal to -21 T for ^{93}Nb polarization[48]. Also for degenerate carriers in a Fermi gas picture, the Korringa relation[47], $\kappa_{\rm KP} \equiv K^2 T_1 T = (\hbar\gamma_e^2)/(4\pi k_B \gamma_n^2)$, can be used to obtain T_1, where γ_e and γ_n are the electron and nuclear gyromagnetic ratios, respectively. This yields $K = -400$ ppm, and $1/(T_1 T) = 0.052$ s^{-1} K^{-1}. Comparing the latter value to $1/(T_{1,\rm exp}T) = 0.015$ s^{-1} K^{-1} for $T \approx 155$ K as described above, this implies that approximately $(0.015/0.052)^{1/2} = 50\%$ of the total Fermi level density of states resides in Nb d orbitals. DFT calculations[27,41] display an orbital projection at the VB edge more heavily dominated by Fe-based states, however the result obtained here appears reasonable, and a small enhancement of T_1^{-1} relative to the Korringa relation is not surprising. By contrast, for carriers confined to a separate impurity band, much larger departures from Korringa behavior would be expected[50], with the electronic contribution to the specific heat not expected to be consistent with an effective mass picture. Thus this provides strong evidence that the native holes reside at the VB edge at these temperatures. This is inconsistent with a low-carrier compensated model for NbFeSb, however given the observed mobility, it is likely that there would be a large energy-dependence to the electron scattering rate. This situation can lead to sign changes in the Seebeck coefficient[51], such as have been observed in NbFeSb[24,26], thus not requiring changes in carrier type.

Scaled according to the Korringa relation, $T_{1,\rm exp}$ derived for 155 K corresponds to $K = -212$ ppm (using $\kappa_{\rm KP} = 3.05 \times 10^{-6}$ s K for ^{93}Nb). Assuming the corresponding chemical shift, $\delta = 3790$ ppm is temperature independent, we obtain K vs temperature shown as the absolute value in Fig. 9. Also shown in this figure is the quantity and $(\kappa_{\rm KP}/T_1 T)^{1/2}$, which tracks K when the Korringa relation holds. This occurs for temperatures below 80 K where the additional dilute paramagnetic contribution to T_1^{-1} disappears, although below 20 K the curves diverge, with T_1^{-1} assuming an approximate $T_1^{1/2}$ behavior. The latter is consistent with Kondo interactions above the Kondo temperature[52,53], thus it appears that the low-temperature behavior is dominated by carriers interacting with the observed local moments.

As noted above, the activated upturn in T_1^{-1} above 280 K must be associated with an impurity band as identified in other undoped half-Heusler semiconductors[4,54]. In the low-temperature regime, since the Fermi level is located in the VB, this impurity band is empty. With the enhancement of thermopower between 300 and 600 K indicating additional holes excited into the VB[1], the impurity band thus must be located just above the VB maximum. The positive sign of the increased NMR shift at these temperatures is presumably due to impurity band defects having Nb s-character, given the positive Fermi contact hyperfine field[4].

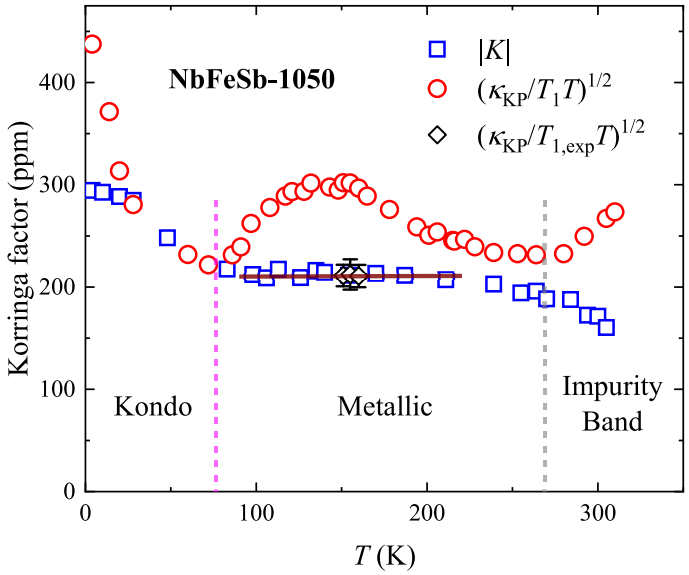

Fig. 9 Dimensionless Korringa factor vs T for sample NbFeSb-1050, with κ_{KP} denoting the theoretical Korringa product.

Considering the nature of the observed defects, Fe antisites on Nb sites appear to be a likely explanation for the observed dilute magnetic defects: the smaller Fe ion has 3 electrons beyond the 5 needed for hybridization on that site. According to crystal field theory, the spin-only magnetic moment of Fe in tetrahedral environment adopts a high-spin $\mu_{so} = \sqrt{4S(S+1)}\mu_B = 3.87\ \mu_B$ with $S = 3/2$. However, this defect would be charge-neutral, so that other defects are needed to explain the observed hole doping. As shown by Yu *et al.*[4], in other 3*d* half-Heusler materials, transition metal interstitials were determined to be the lowest energy defects, as opposed to for example Sb vacancies or other defects, and it was found that an impurity band due to Ni interstitials can explain the gap anomaly in 18-electron ZrNiSb. By analogy it may be that Fe on the half-Heusler interstitial sites form a separate impurity band giving the observed ~0.03 eV activation gap. This band can provide more carriers with increasing temperature, thus explaining the sharp increase of Seebeck coefficient above room temperature[1]. The other likely defect candidate is Nb antisites on Fe sites. Since Nb has 3 fewer valence electrons, and could thus act as a triple acceptor, and such acceptors can pull the chemical potential into the VB and lead to *p*-type metallic behavior at low temperatures. The high resistivity and low mobility of unsubstituted NbFeSb[24,26] can thus be explained by scattering from Nb antisites resonant with the VB.

5 Conclusion

Various techniques including ^{93}Nb NMR, magnetic and specific heat measurements were applied to the half-Heusler semiconductor NbFeSb. The results show a high degree of atomic order, with defects limited to a small density, including a 0.2% uniformly distributed native magnetic defect in NbFeSb samples, likely due to Fe antisites on Nb sites. The NMR shift and spin-lattice relaxation results are consistent with heavily doped *p*-type behavior at low temperatures. The results include a Korringa-type NMR response below 200 K, with constant Knight shift, and a Kondo-related behavior below 80 K due to the interaction of carriers and local moments. Above 280 K, the enhanced Knight shift and T_1^{-1} indicate increased carrier density across a very small gap of about 0.03 eV. Based on this and previously reported transport results, we conclude that this response is associated with an empty impurity band due to acceptor states located a small distance above the valence band maximum, with native *p*-type doping giving the low-temperature metallic behavior.

Conflicts of interest

There are no conflicts to declare.

Acknowledgements

This work done at Texas A&M University is supported by the Robert A. Welch Foundation, Grant No. A-1526 and work done at University of Houston is funded by the U. S. Department of Energy's Basic Energy Science program under Contract DE-SC0010831. Use of the Advanced Photon Source at Argonne National Laboratory was supported by the U. S. Department of Energy, Office of Science, Office of Basic Energy Sciences, under Contract No. DE-AC02-06CH11357.

Notes and references

1 R. He, D. Kraemer, J. Mao, L. Zeng, Q. Jie, Y. Lan, C. Li, J. Shuai, H. S. Kim, Y. Liu *et al.*, *Proc. Natl. Acad. Sci. U.S.A.*, 2016, **113**, 13576–13581.

2 W. Ren, H. Zhu, Q. Zhu, U. Saparamadu, R. He, Z. Liu, J. Mao, C. Wang, K. Nielsch, Z. Wang *et al.*, *Adv. Sci.*, 2018, 1800278.

3 J. Yu, C. Fu, Y. Liu, K. Xia, U. Aydemir, T. C. Chasapis, G. J. Snyder, X. Zhao and T. Zhu, *Adv. Energy Mater.*, 2018, **8**, 1701313.

4 Y. G. Yu, X. Zhang and A. Zunger, *Phys. Rev. B*, 2017, **95**, 085201.

5 S. Bhattacharya and G. K. Madsen, *J. Mater. Chem. C*, 2016, **4**, 11261–11268.

6 M. Zeeshan, H. K. Singh, J. van den Brink and H. C. Kandpal, *Phys. Rev. Materials*, 2017, **1**, 075407.

7 X. Zhang, Y. Wang, Y. Yan, C. Wang, G. Zhang, Z. Cheng, F. Ren, H. Deng and J. Zhang, *Sci. Rep.*, 2016, **6**, 33120.

8 D. A. Ferluccio, R. Smith, J. Buckman and J.-W. Bos, *Phys. Chem. Chem. Phys.*, 2018, **20**, 3979.

9 C. Uher, J. Yang, S. Hu, D. T. Morelli and G. P. Meisner, *Phys. Rev. B*, 1999, **59**, 8615.

10 M. Wambach, R. Stern, S. Bhattacharya, P. Ziolkowski, E. Müller, G. K. Madsen and A. Ludwig, *Adv. Electron. Mater.*, 2016, **2**, 21500208.

11 G. J. Snyder and E. S. Toberer, *Nat. Mater.*, 2008, **7**, 105.

12 M. Kouacou, J. Pierre and R. Skolozdra, *J. Phys. Condens. Matter*, 1995, **7**, 7373.

13 J. Pierre, R. Skolozdra, J. Tobola, S. Kaprzyk, C. Hordequin, M. Kouacou, I. Karla, R. Currat and E. Lelievre-Berna, *J. Alloys Compd.*, 1997, **262**, 101–107.

14 J. Tobola, J. Pierre, S. Kaprzyk, R. Skolozdra and M. Kouacou, *J. Phys. Condens. Matter*, 1998, **10**, 1013.

15 F. Aliev, N. Brandt, V. Moshchalkov, V. Kozyrkov, R. Skolozdra and A. Belogorokhov, *Z. Phys.*, 1989, **75**, 167–171.

16 F. Aliev, V. Kozyrkov, V. Moshchalkov, R. Scolozdra and K. Durczewski, *Z. Phys.*, 1990, **80**, 353–357.

17 D. Young, P. Khalifah, R. Cava and A. Ramirez, *J. Appl. Phys.*, 2000, **87**, 317–321.

18 H. C. Kandpal, C. Felser and R. Seshadri, *J. Phys. D.*, 2006, **39**, 776.

19 T. Graf, C. Felser and S. S. Parkin, *Prog. Solid State Chem.*, 2011, **39**, 1–50.

20 H. Hohl, A. P. Ramirez, C. Goldmann, G. Ernst, B. Wölfing and E. Bucher, *J. Phys. Condens. Matter*, 1999, **11**, 1697.

21 C. Shi, X. Xi, Z. Hou, X. Zhang, G. Xu, E. Liu, W. Wang, W. Wang, J. Chen and G. Wu, *Phys. Status Solidi*, 2015, **252**, 357–360.

22 B. Nowak and D. Kaczorowski, *J. Phys. Chem. C*, 2014, **118**, 18021–18026.

23 X. Zhang, Z. Hou, Y. Wang, G. Xu, C. Shi, E. Liu, X. Xi, W. Wang, G. Wu and X.-X. Zhang, *Sci. Rep.*, 2016, **6**, 23172.

24 A. Tavassoli, F. Failamani, A. Grytsiv, G. Rogl, P. Heinrich, H. Müller, E. Bauer, M. Zehetbauer and P. Rogl, *Acta Mater.*, 2017, **135**, 263–276.

25 C. B. H. Evers, C. G. Richter, K. Hartjes and W. Jeitschko, *J. Alloys Compd.*, 1997, **252**, 93–97.

26 G. Melnyk, E. Bauer, P. Rogl, R. Skolozdra and E. Seidl, *J. Alloys Compd.*, 2000, **296**, 235–242.

27 W. Li, G. Yang and J. Zhang, *J. Phys. D*, 2016, **49**, 195601.

28 A. Roy, J. W. Bennett, K. M. Rabe and D. Vanderbilt, *Phys. Rev. Lett.*, 2012, **109**, 037602.

29 N. F. Mott, *Metal-Insulator Transitions*, Taylor & Francis, London, London, 1990.

30 J. Mason, *Polyhedron*, 1989, **8**, 1657–1668.

31 A. Grykałowska and B. Nowak, *Solid State Nucl. Magn. Reson.*, 2005, **27**, 223–227.

32 T. Harmening, H. Eckert and R. Pöttgen, *Solid State Sci.*, 2009, **11**, 900–906.

33 D. Li, H. Zhao, S. Li, B. Wei, J. Shuai, C. Shi, X. Xi, P. Sun, S. Meng, L. Gu *et al.*, *Adv. Funct. Mater.*, 2015, **25**, 6478–6488.

34 S. Ageev and B. Sanctuary, *Mol. Phys.*, 1995, **84**, 835–844.

35 R. E. Walstedt and L. R. Walker, *Phys. Rev. B*, 1974, **9**, 4857.

36 C. S. Lue, J. H. Ross, Jr., K. D. D. Rathnayaka, D. G. Naugle, S. Y. Wu and W.-H. Li, *J. Phys. Condens. Matter*, 2001, **13**, 1585.

37 C. S. Lue, Y. Li, J. H. Ross, Jr. and G. M. Irwin, *Phys. Rev. B*, 2003, **67**, 224425.

38 D. Tse and S. Hartmann, *Phys. Rev. Lett.*, 1968, **21**, 511.

39 J. V. Kranendonk and M. Walker, *Can. J. Phys.*, 1968, **46**, 2441–2461.

40 R. Dupree, D. J. Kirby and W. W. Warren Jr, *Phys. Rev. B*, 1985, **31**, 5597.

41 T. Fang, S. Zheng, H. Chen, H. Cheng, L. Wang and P. Zhang, *RSC Adv.*, 2016, **6**, 10507–10512.

42 A. Hong, L. Li, R. He, J. Gong, Z. Yan, K. Wang, J.-M. Liu and Z. Ren, *Sci. Rep.*, 2016, **6**, 22778.

43 O. M. Abid, S. Menouer, A. Yakoubi, H. Khachai, S. B. Omran, G. Murtaza, D. Prakash, R. Khenata and K. Verma, *Superlattices Microstruct.*, 2016, **93**, 171–185.

44 G. J. Poon, *Semiconduct. Semimet.*, 2001, **70**, 37–75.

45 C. S. Lue, J. H. Ross, Jr., C. F. Chang and H. D. Yang, *Phys. Rev. B*, 1999, **60**, R13941.

46 C. Çoban, K. Çolakoğlu and Y. Ö. Çiftçi, *Phys. Scr.*, 2015, **90**, 095701.

47 G. C. Carter, L. H. Bennett and D. Kahan, *Metallic shifts in NMR: a review of the theory and comprehensive critical data compilation of metallic materials*, Pergamon, New York, 1977.

48 Y. Yafet and V. Jaccarino, *Phys. Rev.*, 1964, **133**, A1630.

49 N. W. Ashcroft and N. D. Mermin, *Solid state physics*, Holt, Rinehart, and Winston, New York, 1976.

50 S. E. Fuller, E. M. Meintjes and W. W. Warren Jr, *Phys. Rev. Lett.*, 1996, **76**, 2806.

51 P. Sun, B. Wei, J. Zhang, J. M. Tomczak, A. Strydom, M. Søndergaard, B. B. Iversen and F. Steglich, *Nat. Commun.*, 2015, **6**, 7475.

52 D. Cox, N. Bickers and J. Wilkins, *J. Appl. Phys.*, 1985, **57**, 3166–3168.

53 A. P. Dioguardi, P. Guzman, P. F. S. Rosa, N. J. Ghimire, S. Eley, S. E. Brown, J. D. Thompson, E. D. Bauer and F. Ronning, *Phys. Rev. B*, 2017, **96**, 245132.

54 Y. Tang, X. Li, L. H. Martin, E. C. Reyes, T. Ivas, C. Leinenbach, S. Anand, M. Peters, G. J. Snyder and C. Battaglia, *Energy Environ. Sci.*, 2018, **11**, 311–320.